

Cloud-cloud collision and star formation in G323.18+0.15

Yingxiu Ma^{1,2}, Jianjun Zhou^{1,3,4}, Jarken Esimbek^{1,3,4}, Willem Baan^{1,5}, Dalei Li^{1,3,4}, Yuxin He^{1,3,4}, Xindi Tang^{1,3,4},
Weiguang Ji^{1,3,4}, Dongdong Zhou^{1,3,4}, Gang Wu⁶, and Ye Xu⁷

¹ XingJiang Astronomical Observatory, Chinese Academy of Sciences, Urumqi 830011, PR China
e-mail: mayingxiu@xao.ac.cn; zhoujj@xao.ac.cn

² University of Chinese Academy of Sciences, Beijing 100049, PR China

³ Key Laboratory of Radio Astronomy, Chinese Academy of Sciences, Urumqi 830011, PR China

⁴ Xinjiang Key Laboratory of Radio Astrophysics, Urumqi 830011, PR China

⁵ Netherlands Institute for Radio Astronomy, ASTRON, 7991 PD Dwingeloo, The Netherlands

⁶ Max-Planck-Institut für Radioastronomie, Auf dem Hügel 69, D-53121 Bonn, Germany

⁷ Purple Mountain Observatory, Chinese Academy of Sciences, Nanjing 210008, PR China

May 26, 2022

ABSTRACT

We studied the cloud-cloud collision candidate G323.18+0.15 based on signatures of induced filaments, clumps, and star formation. We used archival molecular spectrum line data from the SEDIGISM ¹³CO ($J = 2-1$) survey, from the Mopra southern Galactic plane CO survey, and infrared to radio data from the GLIMPSE, MIPS, Hi-GAL, and SGPS surveys. Our new result shows that the G323.18+0.15 complex is 3.55 kpc away from us and consists of three cloud components, G323.18a, G323.18b, and G323.18c. G323.18b shows a perfect U-shape structure, which can be fully complemented by G323.18a, suggesting a collision between G323.18a and the combined G323.18bc filamentary structure. One dense compressed layer (filament) is formed at the bottom of G323.18b, where we detect a greatly increased velocity dispersion. The bridge with an intermediate velocity in a position-velocity diagram appears between G323.18a and G323.18b, which corresponds to the compressed layer. G323.18a plus G323.18b as a whole are probably not gravitationally bound. This indicates that high-mass star formation in the compressed layer may have been caused by an accidental event. The column density in the compressed layer of about $1.36 \times 10^{22} \text{ cm}^{-2}$ and most of the dense clumps and high-mass stars are located there. The average surface density of class I and class II young stellar objects (YSOs) inside the G323.18+0.15 complex is much higher than the density in the surroundings. The timescale of the collision between G323.18a and G323.18b is 1.59 Myr. This is longer than the typical lifetime of class I YSOs and is comparable to the lifetime of class II YSOs.

Key words. ISM: clouds - ISM: kinematics and dynamics - ISM: individual objects (G323.18+0.15) - radio lines: ISM - stars: formation

1. Introduction

While high-mass star formation is currently poorly understood, two main mechanisms for high-mass star formation have been proposed: the competitive accretion in a massive self-gravitating system (Bonnell et al. 2001), and the monolithic collapse of a dense cloud (McKee & Tan 2002; Krumholz et al. 2009). Both mechanisms have their problems (Fukui et al. 2020). For example, the first cannot explain the formation of single isolated O-stars with a lower system mass (Ascenso 2018). The second requires that the compact cloud or clump produces a column density $\geq 1 \text{ g cm}^{-2}$ (Krumholz et al. 2009, 2012), but it is not clear how such a high-density molecular cloud is formed. If the timescale of forming a high-density cloud is comparable to the free-fall timescale, low-mass stars will form first when the cloud density is high enough, and they may prevent the formation of high-mass stars (Fukui et al. 2020). Therefore, high-density clouds have to be formed in a time much shorter than the free-fall time. Rapid external compression provides an alternative scenario for creating such high-density clouds in a very short time (Zinnecker & Yorke 2007).

Cloud-cloud collisions (CCCs) can result in the rapid accumulation of cloud mass into a small volume and form massive star-forming clumps within the shock interface (Inoue & Fukui 2013; Takahira et al. 2014, 2018; Fukui et al. 2020). This pro-

vides a promising mechanism that can explain isolated or asymmetric O-star formation and the production of dense and massive clumps forming high-mass stars (Fukui et al. 2020). Previous observations have identified more than 50 high-mass star formation regions with collisional features, but more studies are needed to fully understand the detailed properties of colliding clouds and the high-mass star formation triggered by the CCCs.

The G323.18+0.15 complex (see Fig.1) has been studied as component F in the G323 region using data from the Mopra 22m single-dish telescope survey of the southern Galactic plane (Burton et al. 2013). The results suggest that the G323.18+0.15 complex has a system velocity of -65 km s^{-1} and a distance of 4.8 kpc. Its gas mass and column density are about $1.9 \times 10^4 M_{\odot}$ and $9.4 \times 10^{21} \text{ cm}^{-2}$. However, the kinematics of the region has not been studied in detail.

In this paper, we study the kinematics of the G323.18+0.15 complex. We suggest that it may be a good candidate of a CCC complex. We describe the data we used in Sect. 2 and present the physical parameters of the cloud region in Sect. 3. Sect. 4 discusses the evidence of CCCs and the possible effects from an associated H_{II} region. Finally, Sect. 5 gives the conclusion of our work.

2. Archive data

2.1. ^{12}CO and ^{13}CO data

For a kinematic analysis, data of the Structure, Excitation and Dynamics of the Inner Galactic Interstellar Medium (SEDIGISM^{*}) survey have been used (Schuller et al. 2021). This survey mapped 84 deg^2 of the Galactic plane ($-60^\circ < l < 31^\circ$, $|b| < 0.5^\circ$) with the Atacama Pathfinder Experiment (APEX) telescope in several molecular transitions, including $^{13}\text{CO}(J=2-1)$ and $\text{C}^{18}\text{O}(J=2-1)$. The angular resolution of SEDIGISM is $\sim 30''$, and the 1σ sensitivity is about 0.8–1.0 K for a 0.25 km s^{-1} channel width. The $^{12}\text{CO}(J=1-0)$ data from the Mopra 22m single-dish telescope survey of the southern Galactic plane (Burton et al. 2013) has also been used, which has a spatial resolution of $35''$ and the 1σ sensitivity of 1.5 K per 0.1 km s^{-1} velocity channel.

2.2. IR and radio data

We used the image data from the Galactic Legacy Infrared Mid-Plane Survey Extraordinaire (GLIMPSE) (Churchwell et al. 2009) to derive the mid-infrared emission at 3.6, 4.5, 5.8, and $8\mu\text{m}$. The 5σ sensitivities at the four bands are 0.2, 0.2, 0.4, and 0.4 mJy , respectively. The corresponding angular resolutions are between $1.5''$ and $1.9''$ (Fazio et al. 2004). We also used the image data from the Multiband Infrared Photometer for Spitzer MIPS Galactic Plane Survey (MIPSGAL) (Carey et al. 2009) at 24 and $70\mu\text{m}$ with a 5σ sensitivity of 1.7 mJy and with corresponding resolutions of $6''$ and $18''$, respectively (Rieke et al. 2004).

We used Herschel Infrared Galactic Plane Survey (Hi-GAL, Molinari et al. (2010)) data to derive the dust temperature and column density distributions. Hi-GAL is a key project of the 3.5 m orbiting Herschel telescope as it mapped the entire Galactic plane within $|b| < 1^\circ$ at five bands. The angular resolutions of these Herschel maps are approximately $10.2''$, $13.5''$, $18.1''$, $25.0''$, and $36.4''$ at 70, 160, 250, 350, and $500\mu\text{m}$, respectively.

The 1.4 GHz radio continuum emission data from the Southern Galactic Plane Survey (SGPS, Haverkorn et al. (2006)) were used to trace H_{II} regions, which was observed with the Australia Telescope Compact Array and the Parkes 64 m single-dish telescope. The survey spans a Galactic longitude of $253^\circ < l < 358^\circ$ and a latitude of $|b| < 1.5^\circ$ at a resolution of $100''$ and a sensitivity below 1 mJy beam^{-1} .

2.3. Catalogs

The APEX Telescope Large Area Survey of the Galaxy (ATLASGAL) dense clump catalog (Urquhart et al. 2018) and the Herschel Hi-GAL clump catalog (Elia et al. 2017) were used to trace dense clumps. The GLIMPSE Point-Source catalog (GPSC) is used to trace the young stellar objects (YSOs).

* This publication is mainly based on data acquired with the Atacama Pathfinder Experiment (APEX) under programs 092.F-9315(A) and 193.C-0584(A). APEX is a collaboration between the Max-Planck-Institut für Radioastronomie, the European Southern Observatory, and the Onsala Space Observatory. The processed data products are available from the SEDIGISM survey database located at <https://sedigism.mpifr-bonn.mpg.de/index.html>, which was constructed by James Urquhart and is hosted by the Max-Planck-Institut für Radioastronomie.

3. Results

3.1. G323.18+0.15 complex

The distributions of the integrated $^{12}\text{CO}(1-0)$ and $^{13}\text{CO}(2-1)$ emission of the G323.18+0.15 complex are shown on a background of the $250\mu\text{m}$ dust emission in Fig. 1. The distributions of $^{12}\text{CO}(J=1-0)$ and $^{13}\text{CO}(J=2-1)$ agree well with that of the $250\mu\text{m}$ dust emission. The $^{13}\text{CO}(J=2-1)$ map of the G323.18+0.15 complex shows separate northwestern and southeastern components, while the $^{12}\text{CO}(J=1-0)$ map shows that these components are connected to each other. Fig. 2 presents more observation results of the G323.18+0.15 complex (right panel) and nearby H_{II} regions (left panel) at different wavelengths. White circles denote the H_{II} regions identified by Anderson et al. (2014), and red background traces the 21cm continuum emission. The H_{II} region G323.187+00.129 is right in between the northwestern and southeastern components of the G323.18+0.15 complex. The $8\mu\text{m}$ emission appears in all H_{II} regions. In the region we studied, class I (pink crosses) and class II (yellow triangles) YSOs mainly lie on the G323.18+0.15 complex or nearby it.

Considering the high resolution and good data quality of $^{13}\text{CO}(J=2-1)$, we mainly used $^{13}\text{CO}(J=2-1)$ in the following analysis. Using the system velocity -65.75 km s^{-1} derived from the averaged $^{13}\text{CO}(J=2-1)$ spectrum of the G323.18+0.15 complex and the new kinematic distance estimator** developed by Reid et al. (2019), we obtain a distance of about $3.55\pm 0.45\text{ kpc}$. This is smaller than the earlier distance of 4.8 kpc obtained by Burton et al. (2013). Because the latest distance estimator is based on the much improved rotation curve of the Galaxy, we use the newer distance of G323.18+0.15 complex in this work.

3.2. Column density and dust temperature

First, we removed the background emission from the image data at different bands separately. Then we used the kernels provided by Aniano et al. (2011) to convolve all images at 70, 160, 250, and $350\mu\text{m}$ to the angular resolution $36.4''$ at $500\mu\text{m}$. Finally, we regridded all images at five bands to the same pixel size ($11.5''$), and performed a spectral energy distribution fit pixel by pixel with the PYTHON package HIGAL-sed-fitter***. The code is based on a modified blackbody model,

$$I_\nu = B_\nu(1 - e^{-\tau_\nu}), \quad (1)$$

where the Planck function B_ν is modified by the optical depth (Kauffmann et al. 2008),

$$\tau_\nu = \mu_{\text{H}_2} m_{\text{H}} K_\nu N_{\text{H}_2} / R_{\text{gd}}, \quad (2)$$

where $\mu_{\text{H}_2} = 2.8$ is the mean molecular weight, m_{H} is the mass of a hydrogen atom, the gas to-dust ratio is $R_{\text{gd}} = 100$, and N_{H_2} is the H_2 column density. The dust opacity (Ossenkopf & Henning 1994) is

$$K_\nu = 4.0(\nu/505\text{ GHz})^\beta \text{ cm}^2\text{ g}^{-1}, \quad (3)$$

and the dust emissivity index β was fixed to 1.75 in the fitting (Wang et al. 2015).

The derived H_2 column density (N_{H_2}) and dust temperature are shown in Fig. 3. N_{H_2} varies from 1.0×10^{20} to $1.4 \times 10^{22}\text{ cm}^{-2}$ with a mean value of $4.0 \times 10^{21}\text{ cm}^{-2}$. The densest structure was

** <http://bessel.vlbi-astrometry.org/node/378>

*** <http://hi-gal-sed-fitter.readthedocs.org>

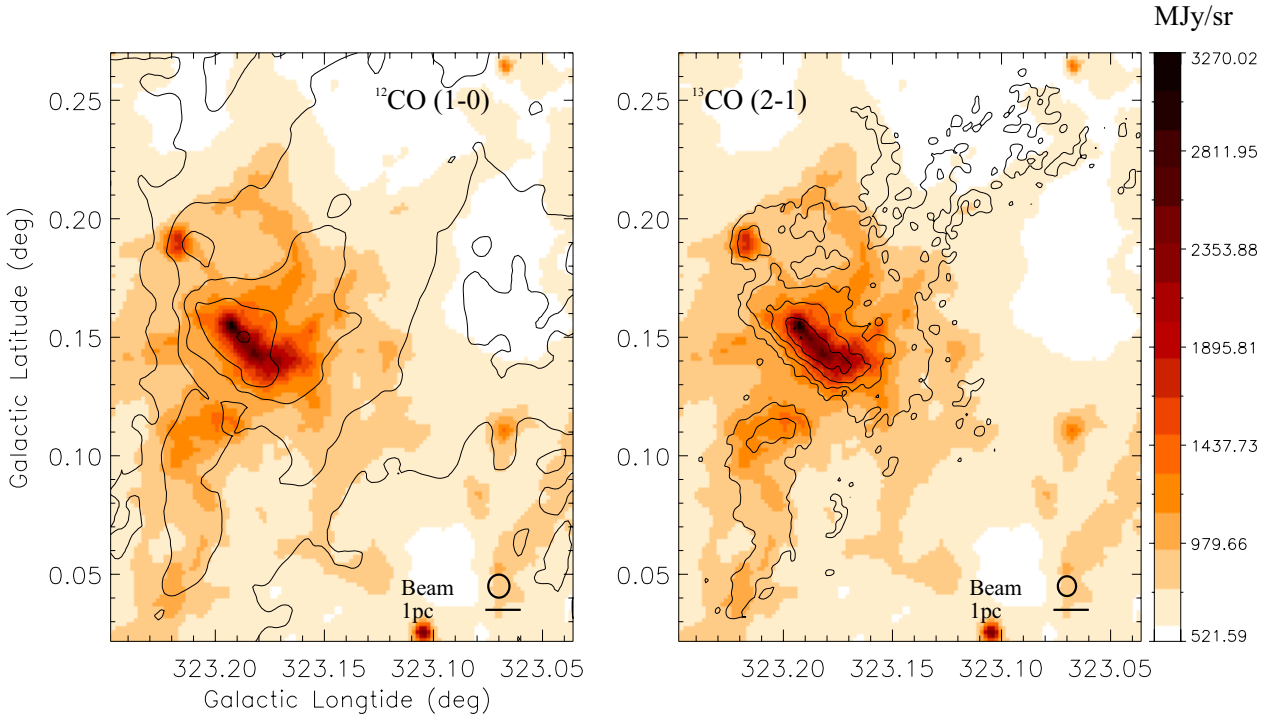


Fig. 1. G323.18+0.15 complex region imaged by Herschel at $250\mu\text{m}$. The black contours represent the $^{12}\text{CO}(J=1-0)$ (left) emission and $^{13}\text{CO}(J=2-1)$ (right) emission integrated from -69 to -61 km s^{-1} . The contour levels start from 6 and 2 K km s^{-1} and increase in steps of 8 and 11 K km s^{-1} , respectively.

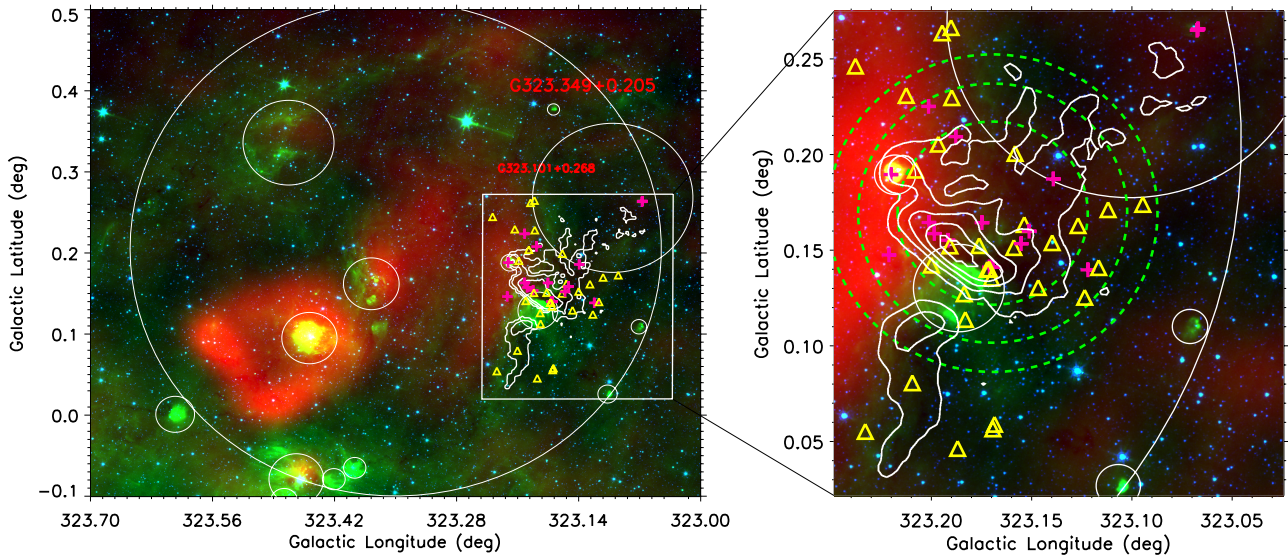


Fig. 2. Three-color map of the G323.18+0.15 complex (right) and nearby H_{II} regions (left). Left: Red, green, and blue background shows 21 cm , $8\mu\text{m}$, and $4.5\mu\text{m}$ emission, respectively. The white circles are the H_{II} regions identified by Anderson et al. (2014). The white rectangular box is the research region, a zoom of which is shown in the right panel. The white contours are the integral intensity of the ^{13}CO emission from -69 to -61 km s^{-1} in the G323.18+0.15 complex. The white crosses and yellow triangles are class I and II YSOs, respectively. Right: Same as the left panel, but the dashed green circles are the area for which the surface density was calculated (see sect. 4.2).

identified as filament G323.179+0.149 by Li et al. (2016). We plot its skeleton as the dot-dashed white line in Fig 3. Twenty-one highly reliable clumps from the Herschel Hi-GAL clump catalog (Elia et al. 2017) and three clumps from the ATLAS-GAL dense clump catalog (Urquhart et al. 2018) are located

in the region we studied (their evolutionary stages and parameters are listed in table. 1). Because HIGALBM323.1050+0.0241 and AGAL323.104+0.024, HIGALBM323.1923+0.1539 and AGAL323.192+0.154 are the identical sources, there are a total of 22 clumps in the region we studied.

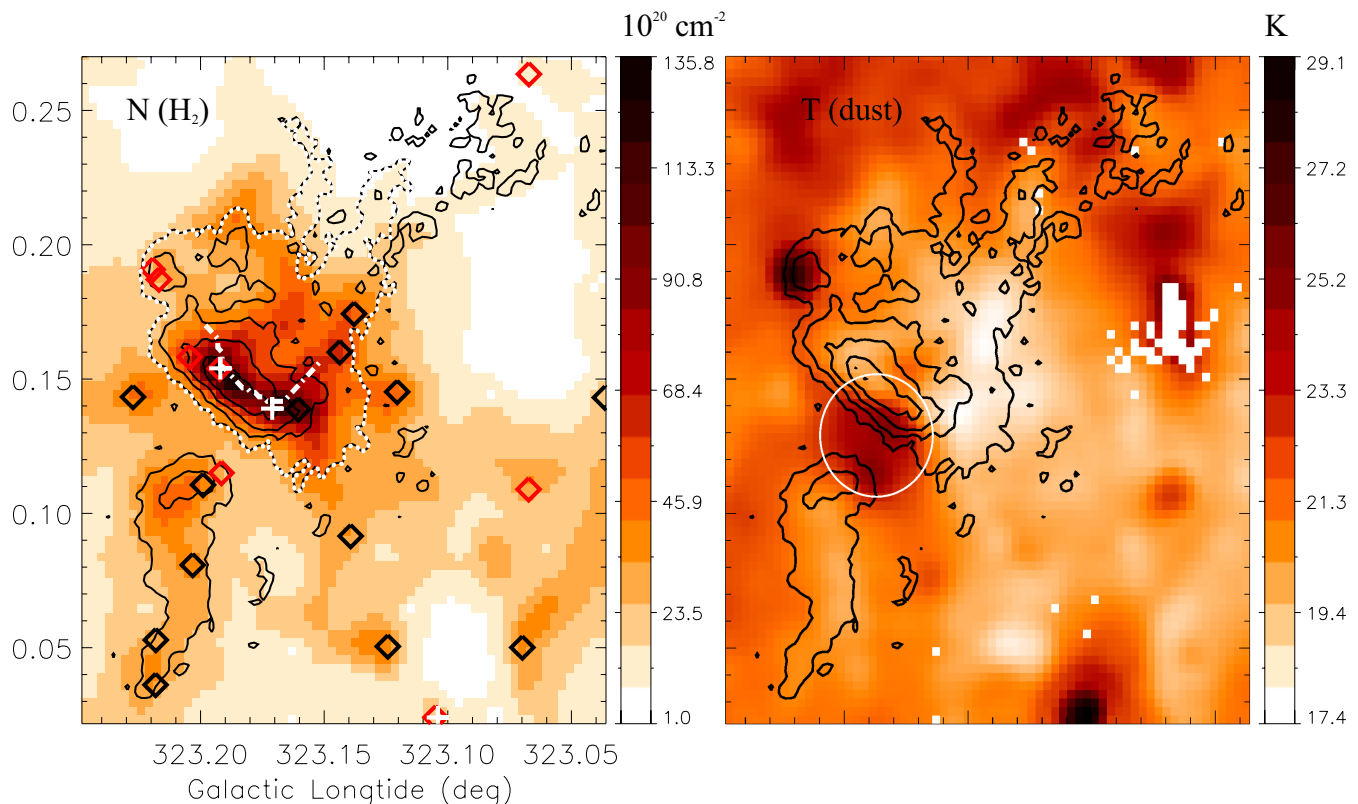


Fig. 3. Column density (left) and temperature (right) distributions within the G323.18+0.15 complex. The black contours indicate the ^{13}CO ($J=2-1$) integrated intensity in areas where T_{mb} is higher than 3σ (3 K). The contour levels start from 2 K km s^{-1} and increase in steps of 11 K km s^{-1} . The velocity interval of the integration is -69 to -61 km s^{-1} . The region surrounded by the dotted white line is used for the calculations in sect. 4.1. The dot-dashed white line is the skeleton of filament G323.179+0.149 identified by Li et al. (2016). The black and red diamonds are prestellar and protostellar clumps from the Herschel HIGAL clump catalog, and the white crosses are ATLASGAL $870\text{ }\mu\text{m}$ clumps (see table. 1 for details). The white circle in the right panel is the H_{II} region G323.187+00.129 identified by Anderson et al. (2014).

The dust temperature of the G323.18+0.15 complex is relatively low (right panel of Fig. 3). This is especially true for the northwestern part. The H_{II} region G323.187+00.129, located between the northwestern and southeastern part, which was identified by Anderson et al. (2014), has a higher temperature.

3.3. Structure and kinematics

The ^{13}CO ($J=2-1$) velocity channel maps in Fig. 4 suggest the presence of three cloud components in the G323.18+0.15 complex with different velocities: G323.18a with a velocity range from -69.0 to -65.5 km s^{-1} , the U-shaped structure G323.18b with a velocity range from -65.5 to -63.75 km s^{-1} , and G323.18c with a velocity range from -64.0 to -62.0 km s^{-1} . The system velocities of G323.18a, G323.18b, and G323.18c are estimated to be -67.25 , -64.63 , and -63 km s^{-1} , respectively. The intensity-weighted velocity field of the ^{13}CO ($J=2-1$) emission (top left panel of Fig. 5) also shows the same three components.

Figure 6 shows the velocity-integrated intensity map of ^{13}CO ($J=2-1$) for G323.18a, G323.18b, and G323.18c. It clearly shows the locations and structures of these three molecular cloud components. G323.18b appears to be a perfect U-shape structure with a compressed layer (the filament G323.179+0.149; Li et al. (2016)) with high-mass clumps in which high-mass stars are expected to form. The highest ve-

locity dispersion also appears in the compressed layer, implying that there is strong turbulent activity (see the top right panel of Fig. 5). G323.18a is complementary to G323.18b. Some ^{13}CO ($J=2-1$) emission of G323.18c appears at the location of G323.18b, and the H_{II} region G323.187+00.129 interacts with both G323.18b and G323.18c. This indicates that G323.18b and G323.18c are connected to each other. ^{12}CO ($J=1-0$) in Fig. 1 also shows that they are in the same molecular cloud. As seen in the partially enlarged plot at the top of Fig. 6, the green $8\text{ }\mu\text{m}$ emission seems to be blowing out at the southeastern side of the dark filament, and the red $24\text{ }\mu\text{m}$ emission appears close to the southeastern side of the dark filament. High-mass stars appear to be forming in the compressed layer and contribute to exciting the H_{II} region G323.187+00.129 (Anderson et al. 2014). Most of the strong 8 and $24\text{ }\mu\text{m}$ emission seems to be wrapped inside G323.18b, which also supports this idea.

We show the ^{13}CO ($J=2-1$) position-velocity (PV) diagram in the bottom panel of Fig. 5. The PV slice is extracted along the red line labeled in the top panels of Fig. 5 and shows that G323.18c is separated from G323.18a and G323.18b, which may be because H_{II} region G323.187+00.129 (Anderson et al. 2014) blows off diffuse gas between them. The vertical dotted line along the offset axis corresponds to the position of the red circle on the red line in the top panels of Fig. 5, which identifies the compressed layer, that is, the interface between G323.18a

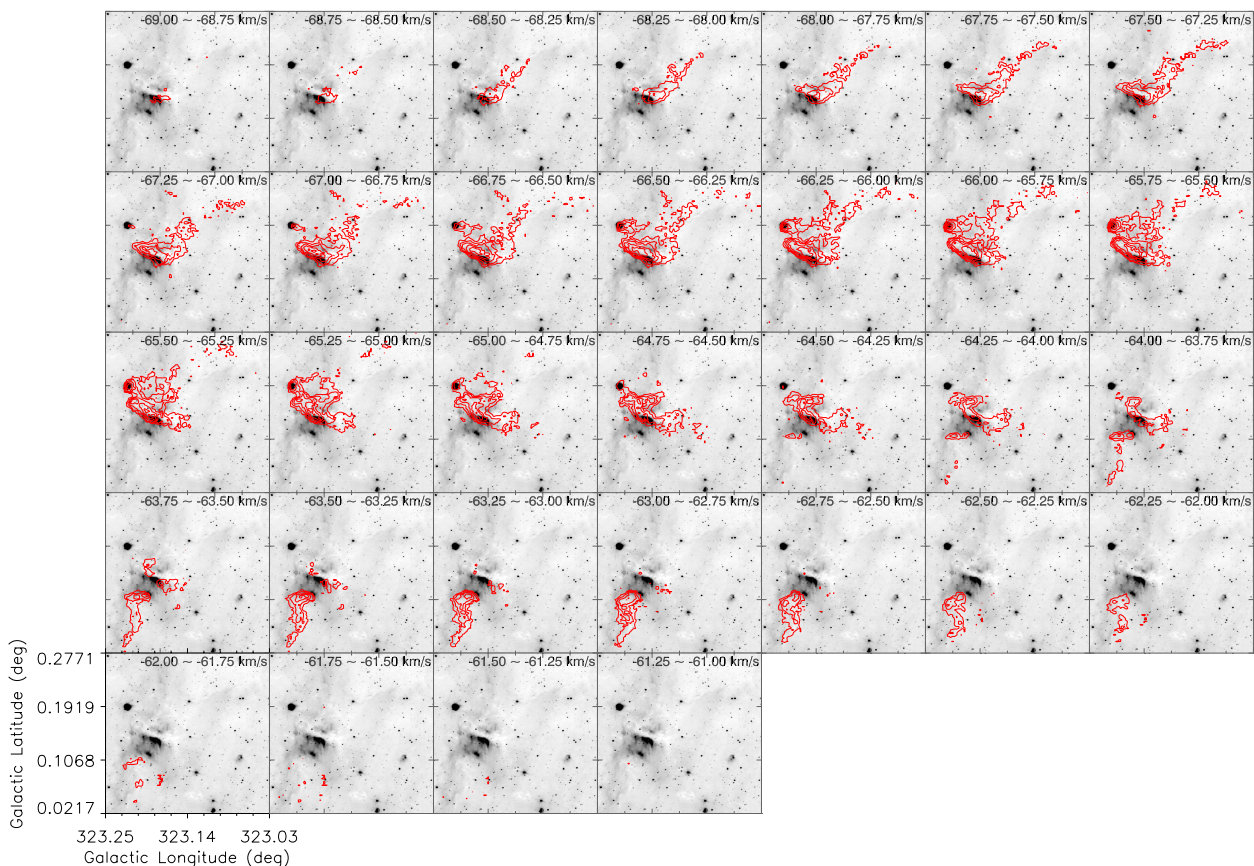


Fig. 4. Channel maps of the ^{13}CO ($J=2-1$) emission for G323.18+0.15 complex (red contours) with contour levels at 3, 5, 7, 9, and 11 K km s^{-1} . The background is the Spitzer $8\ \mu\text{m}$ emission map.

and G323.18b. Strong CO emission appears between the system velocities of G323.18a and G323.18b, indicating that most of the CO from these two clouds is sufficiently mixed in the compressed layer.

The upper panels of Fig. 7 show the integral intensity maps of ^{13}CO ($J=2-1$) corresponding to the velocity ranges from -64.63 to $-63\ \text{km s}^{-1}$ (left panel), -67.25 to $-64.63\ \text{km s}^{-1}$ (middle panel), and -69 to $-67.25\ \text{km s}^{-1}$ (right panel). Their morphology indicates that the two clouds in the left and right panels may be interacting with each other, while the cloud in the middle panel is the result of this interaction. The lower panels show a $3 \times ^{12}\text{CO}$ ($J=1-0$), $1.5 \times ^{13}\text{CO}$ ($J=2-1$), and $1.5 \times \text{C}^{18}\text{O}$ ($J=2-1$) spectrum extracted at the positions indicated by the white circles in the corresponding upper panels. The ^{13}CO and C^{18}O spectra in the right and left panels peak at the estimated system velocities of -67.25 (G323.18a) and $-64.63\ \text{km s}^{-1}$ (G323.18b), while the ^{13}CO and C^{18}O spectra in the middle panel peak at an intermediate velocity between these two system velocities. This is consistent with the above result, that is, the cloud in the middle panel is formed through an interaction between the two clouds in the left and right panels, which causes the two initial clouds to appear as a single-peaked continuous cloud.

Two additional components lie at ~ -52 and $-30\ \text{km s}^{-1}$, which are partly overlaid on G323.18b in projection. Because they are very weak and their velocities are very different from that of the G323.18+0.15 complex, we assume that these two components just happened to be superimposed on the

G323.18+0.15 complex along the line of sight, and we do not show them here.

3.4. YSOs

The multiphase source classification scheme, a slightly modified version of the Gutermuth et al. (2009), has been used to identify YSOs (Zhou et al. 2020; Liu et al. 2015) (see Appendix A for details). A total of 16 class I and 30 class II YSOs have been found in the region we studied (see Fig. 2). Almost all class I YSOs are located in the U-shape structure G323.18b, while the class II YSOs around the U-shape structure also display an arc-like distribution. However, some class II YSOs may be associated with the H_{II} regions near the G323.18+0.15 complex (see Fig. 2 and the discussion in sect. 4.4).

4. Discussion

4.1. Signatures of CCCs

First, we examined whether G323.18a and G323.18b are gravitationally bound as one structure. The virial mass was determined using the expression (Pillai et al. 2011; Issac et al. 2020)

$$M_{\text{vir}} = \frac{5\sigma^2 R}{G}, \quad (4)$$

where R is the effective radius of the cloud and $\sigma = \Delta V / \sqrt{8 \ln 2}$ is the velocity dispersion. Both R and σ were obtained using the ^{13}CO ($J=2-1$) line. R is thought of as $(A/\pi)^{0.5}$, where

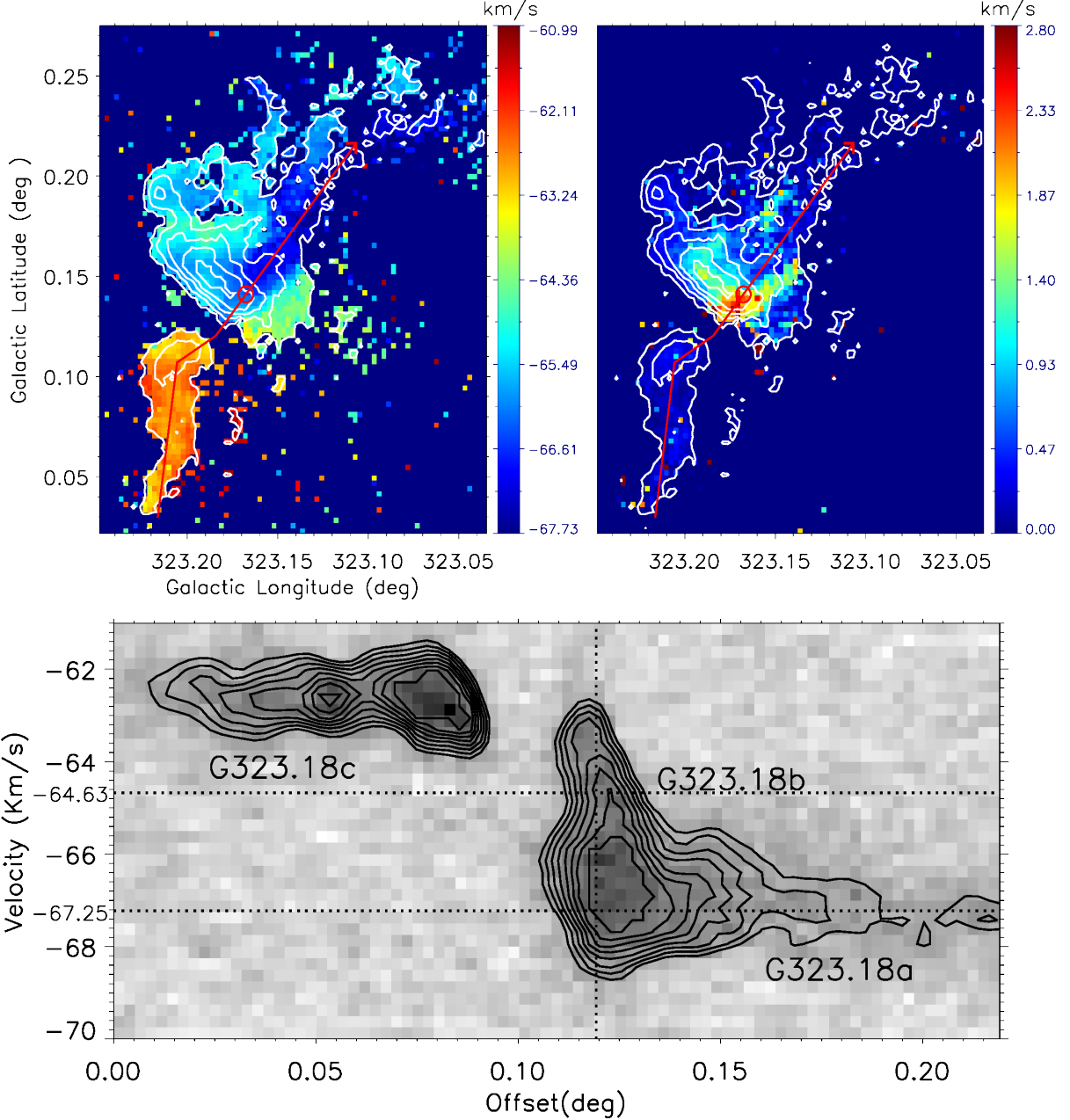


Fig. 5. Moment 1 and Moment 2 of the G323.18+0.15 complex, and PV diagram along its filamentary structure. Top: The color backgrounds in the left and right panels are velocity field and velocity dispersion of ^{13}CO ($J=2-1$). The white contours denote ^{13}CO emission integrated from -69 to -61 km s^{-1} , which starts from 2 K km s^{-1} (signal weaker than 3σ is masked out) and increases in steps of 9 K km s^{-1} . Bottom: Position-velocity diagram of the ^{13}CO ($J=2-1$) emission along the direction labeled by the red line in the top panel. The vertical dotted black line represents the position that is plotted as small red circles in the top panel. The horizontal dotted black lines represent the system velocities of G323.18a and G323.18b. The black contours start at 3 K and increase in steps of 0.9 K .

$A = 26.46 \pm 5 \text{ pc}^2$ is the area used to derive the cloud mass using the area marked with the dotted white line in left panel of Fig. 3. This results in a value of $R = 2.9 \pm 0.31 \text{ pc}$. From a Gaussian fit of the averaged ^{13}CO spectrum of the cloud, we obtained the line width $\Delta V \sim 3.6 \text{ km s}^{-1}$. This results in a value for the velocity dispersion of 1.5 km s^{-1} . Using these values, we computed the virial mass as $7.6 (\pm 0.8) \times 10^3 M_{\odot}$. The total gas mass of G323.18a and G323.18b was calculated using the expression

$$M_{\text{H}_2} = \mu m_{\text{H}} \sum_i S_i N(\text{H}_2)_i, \quad (5)$$

where the mean molecular weight μ is 2.8, the mass of hydrogen atom is $1.67 \times 10^{-24} \text{ g}$, $S_i = (3.7 \pm 0.9) \times 10^{35} \text{ cm}^2$ is one pixel area, and $N(\text{H}_2)_i$ is obtained from the spectral energy distribution fit. We obtain a gas mass of $2.84 (\pm 0.5) \times 10^3 M_{\odot}$, which is lower than the virial mass. This means that G323.18a and G323.18b as a whole cloud are not gravitational bound, which suggests that an accident has triggered the ongoing star formation, for instance, a cloud-cloud collision. We discuss the potential characteristic features of the CCC in the G323.18+0.15 complex in the following subsections, including the complementary distribution

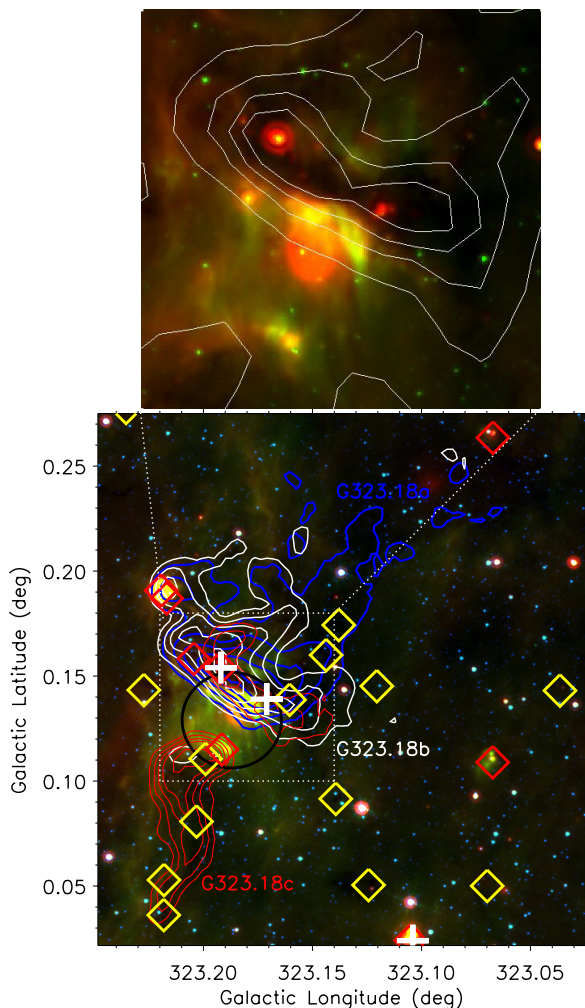


Fig. 6. Velocity-integrated intensity maps of the ^{13}CO ($J=2-1$) emission. Bottom panel: Velocity-integrated intensity map of G323.18a (blue contours integrated from -69.0 to -65.5 km s^{-1} starting at 2 K km s^{-1} with an increment of 5.5 K km s^{-1}), G323.18b (white contours, integrated from -65.5 to 64.0 km s^{-1} starting at 2 K km s^{-1} with an increment of 3.8 K km s^{-1}), and G323.18c (red contours, integrated from -64 to -62 km s^{-1} starting at 2 K km s^{-1} with an increment of 2.3 K km s^{-1}). The black circle denotes H_{II} region G323.187+00.129 identified by Anderson et al. (2014). The yellow and red diamonds are prestellar and protostellar clumps from the Herschel Hi-Gal clump catalog, and the white crosses are ATLASGAL 870 μm clumps. The background is a three-color map with red, green, and blue for 24 , 8 , and 4.5 μm , respectively. Top panel: White contours start from 2×10^{21} cm^{-2} and increase in steps of 1.9×10^{21} cm^{-2} . They display the distribution of the H_2 column density of the dotted rectangle in the bottom panel. The background is the same as in the bottom panel.

with displacement, the U-shape, the bridge and the first moment distribution (Fukui et al. 2018, 2020).

4.1.1. Complementary distribution and U-shape

As shown in Fig. 6, G323.18b displays a perfect U-shape structure, and the cloud G323.18a complements the U-shape well. These two characteristic features suggest that G323.18a indeed collides with G323.18b. Based on the channel map shown in Fig. 4, we estimate the systemic velocities of G323.18a and G323.18b to be -67.25 and -64.63 km s^{-1} . The actual collision velocity might be higher because of projection effects. As pro-

pounded by Issac et al. (2020), Inoue & Fukui (2013), and Fukui et al. (2015), independent of the angle of two colliding clouds, the isotropic turbulence is enhanced at the collision-shocked layer. This is consistent with the fact that the velocity dispersion increases greatly along the U-shape structure (see the top right panel of Fig. 5).

4.1.2. Bridge

Simulations of Haworth et al. (2015a,b) suggested that a broad intermediate-velocity feature that bridges between two colliding clouds will appear in a PV diagram. The bridge feature probes the turbulent motion of the gas enhanced by the collision and often appears at the spots of collisions (Issac et al. 2020; Gong et al. 2017). The increased velocity dispersion along the U-shape, especially at the bottom where the compressed layer formed (see the top right panel of Fig. 5), suggests that the compressed layer is the interface of the collision between G323.18a and G323.18b. The bridge feature with an intermediate velocity between -67.25 and -64.63 km s^{-1} is clearly visible in the PV diagram of G323.18+0.15 in the bottom panel of Fig. 5. The significant bridge feature indicates that G323.18a has interacted with G323.18b and that most of the gas of these two clouds has been compressed into the dense layer at the bottom of U-shape. This idea is also supported by the fact that both ^{13}CO and C^{18}O spectrum from the compressed layer exhibit a single-peak profile between the velocity -67.25 and -64.63 km s^{-1} (see Fig. 7). G323.18b and G323.18a may be in a later stage of CCC. They are very close to each other, and the bridge appears as the efficiently mixed gas of G323.18a and G323.18b.

4.1.3. Distribution of the first moment

Fukui et al. (2018) showed simulation results of one small spherical cloud colliding with another large spherical cloud. If the viewing angle between the line of sight and the direction of the collision is 0° or 45° , the small cloud will appear in the center of the large cloud in the first-moment map. If the viewing angle is 90° , a compressed layer forms (see their Figures 4, 5, 6 and 7). However, this may be not true when the colliding clouds are not spherical. Both G323.18a and G323.18b appear in the first-moment map of ^{13}CO ($J=2-1$) (see the top left panel of Fig. 5), and G323.18a displays an extended filamentary structure that connects it to G323.18b. This suggests that our viewing angle is not 0° and that G323.18a is a filamentary cloud before it collides. Considering that the velocity variation at the interface is relatively small (the bottom panel of Fig. 5) and because the compressed layer at the interface between the two clouds appears as a filament, our viewing angle may be close to 90° ,

4.2. Induced filament, fragmentation of clumps, and star formation

Hydrodynamic simulations (Habe & Ohta 1992; Anathpindika 2010) suggest that the site of a CCC can be characterized by a shock-compressed layer resulting from a bow shock that is driven by the smaller cloud into the larger cloud. In the case of the G323.18+0.15 complex, the shock-compressed layer manifests itself as an open U-shape structure. This U-shape structure has a higher H_2 column density than the ambient medium, as shown in Fig. 3. The compressed layer at the bottom of the U-shape structure is perpendicular to the direction of the collision.

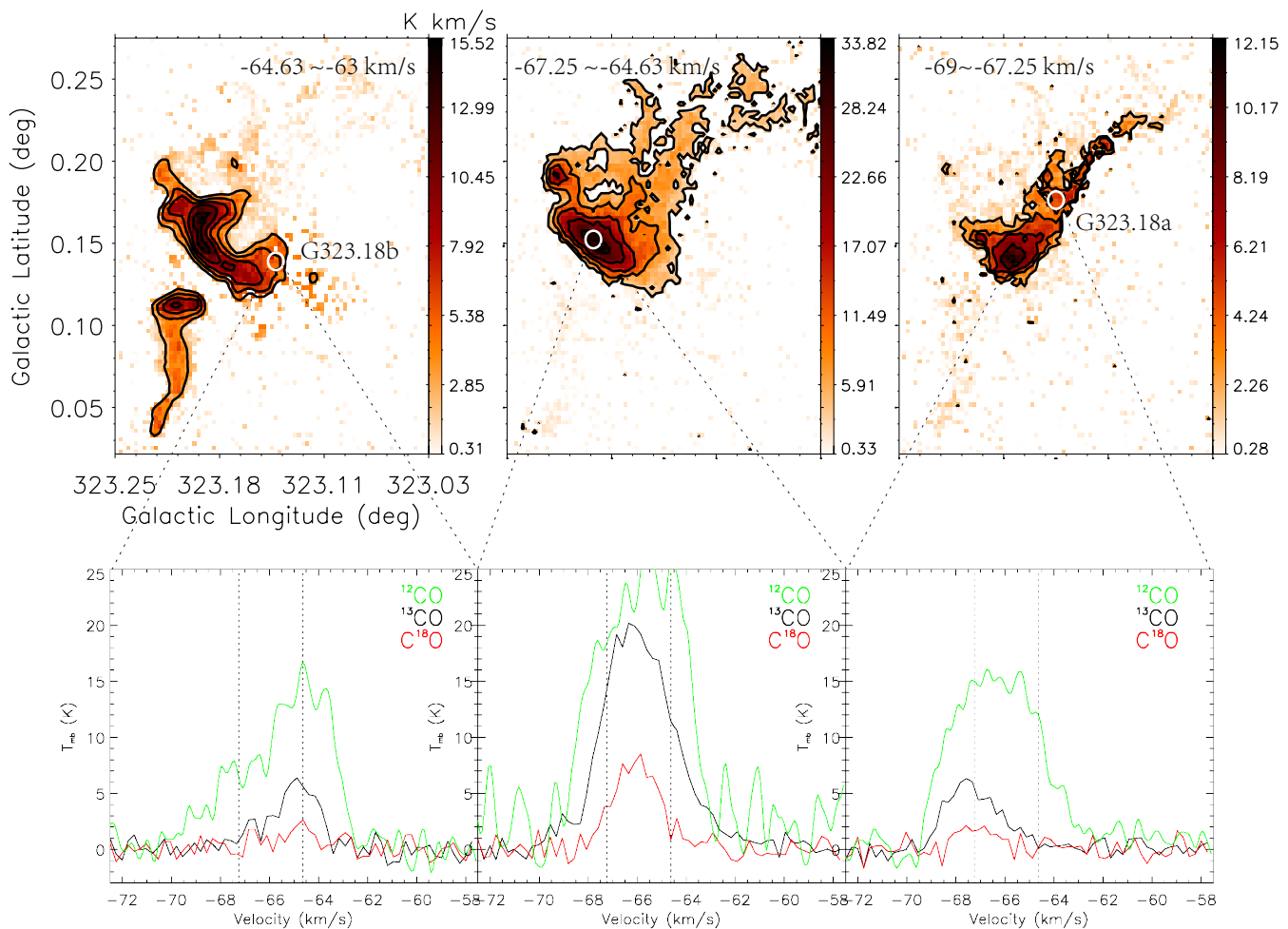


Fig. 7. Spectra of the three regions in G323.18+0.15. The upper panels from left to right are the integral intensities corresponding to the velocity ranges from -64.63 to -63 km s^{-1} , from -67.25 to -64.63 km s^{-1} , and from -69 to -67.25 km s^{-1} . The corresponding black contours start at 3 K km s^{-1} and increase in steps of 2.2 , 6.1 , and 1.3 K km s^{-1} , respectively. The lower panels are for the $3 \times {}^{12}\text{CO}$ ($J=1-0$), $1.5 \times {}^{13}\text{CO}$ ($J=2-1$), and $1.5 \times \text{C}^{18}\text{O}$ ($J=2-1$) spectra extracted at three different positions of the G323.18+0.15 complex, indicated by white circles in the corresponding upper panels. The vertical dashed black lines represent the systemic velocities of G323.18a (-67.25 km s^{-1}) and G323.18b (-64.63 km s^{-1}).

The region we studied contains 22 clumps (see sect. 3.2). Thirteen of these 22 clumps are located in the G323.18+0.15 complex (Figs. 3 and 6), that is, the area covered by ${}^{13}\text{CO}$ ($J=2-1$) emission with a signal-to-noise ratio $S/N > 3$. Their diameters and masses were recalculated using a distance of 3.55 kpc. The masses of these clumps range from 12.65 to $1.7 \times 10^3 M_{\odot}$ and the diameters range from 0.2 to 0.5 pc. Twenty-one clumps have surface densities above the threshold of 0.05 g cm^{-2} (Urquhart et al. 2014) (see table. 1), and they are likely able to form high-mass stars.

A total of 46 YSOs may be found in the whole region we studied using the GPSC (Fig. 2). Eleven of the 16 class I YSOs and 15 of the 30 class II YSOs are located in G323.18+0.15 and in the area covered by ${}^{13}\text{CO}$ ($J=2-1$) emission with $S/N > 3$. Three dashed green circles are plotted in Fig. 2, where the areas of the circle and two annuli are the same as the area that is covered by the molecular clouds G323.18a and G323.18b. The average surface densities of class I and II YSOs in the innermost circle are 0.39 arcmin^{-2} and 0.58 arcmin^{-2} , respectively, but they are 0.16 and 0.19 arcmin^{-2} in the first annulus, and 0 and 0.08 arcmin^{-2} in the second annulus. It is evident that the surface density of YSOs in the interaction region is much higher.

Following Issac et al. (2020), we used the full width at half maximum (FWHM) (3.56 km s^{-1}) of the ${}^{13}\text{CO}$ ($J=2-1$) line extracted from the compressed layer to estimate the relative collision velocity, and calculated the collision timescale of cloud G323.18a and G323.18b. With a cloud size 5.8 pc, a collision timescale of 1.59 ± 0.14 Myr is derived as an order-of-magnitude estimate. This value may vary by a factor of 2 owing to projection effects in space and velocity and to the unknown configuration of the clouds before the collision (Fukui et al. 2014). For comparison, the ages of class I and II YSOs are $0.4 - 0.7$ Myr and 2 ± 1 Myr, respectively (Evans et al. 2009; Dunham et al. 2015; Issac et al. 2020). Our collision timescale of 1.59 Myr exceeds the age of a class I YSO, but would be comparable to that of a class II YSO. This suggests that most YSOs in the G323.18+0.15 complex could have formed as a result of the collision between G323.18a and G323.18b, especially for class I YSOs. To some extent, this is consistent with the hypothesis that a collision triggered the YSOs formation.

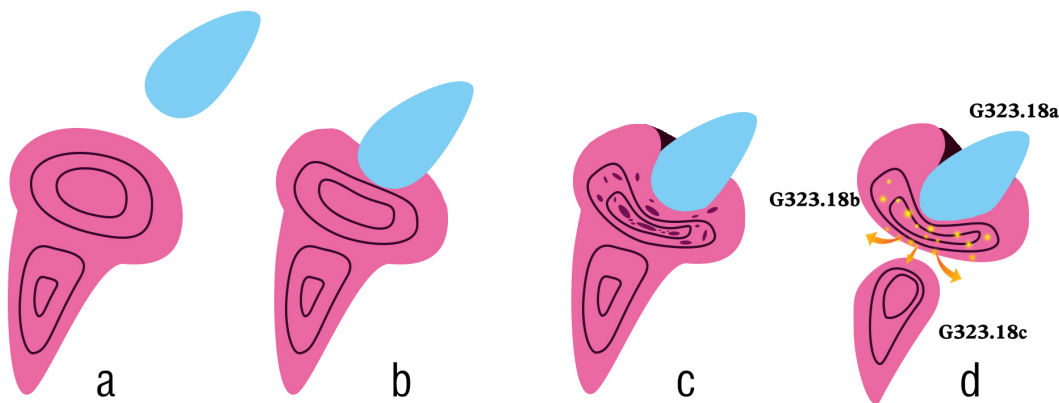


Fig. 8. Schematic of the G323.18+0.15 complex before and after the collision. In panel a, the long blueshifted cloud G323.18a comes from the northwestern direction and collides with G323.18b and G323.18c. In panels b and c, the collision forms a U-shape structure and a dense layer. In panel d, YSOs are forming in the dense compressed layer, and then the strong stellar wind and radiation pressure blow away the sparse gas and dust between G323.18b and G323.18c.

4.3. CCC scenario for the G323.18+0.15 complex

The images in Fig. 8 presents a schema for the evolutionary development of the three cloud components G323.18a, G323.18b, and G323.18c in the G323.18+0.15 complex. Our results suggest that G323.18b and G323.18c belong to the same filamentary cloud and that G323.18a collides with G323.18b. In Fig. 8a, G323.18a comes from the northwestern direction and approaches the filamentary cloud structure, which consists of G323.18b and G323.18c. In Fig. 8b and Fig. 8c, G323.18a collides with G323.18bc and forms a U-shape structure and a compressed dense layer at the bottom of G323.18b. The colliding direction seems to be nearly perpendicular to our line of sight. High-mass stars are forming within the dense layer, and together, they form an H_{II} region that provides strong feedback that first breaks through the parent cloud from the southeastern side of the filament and heats and blows off diffuse gas between G323.18b and G323.18c (Fig. 8d).

4.4. Possible effect from H_{II} regions

Although we find characteristic features of a CCC in G323.18+0.15, it is difficult to fully rule out other possibilities. There are five H_{II} regions in the region we studied, as identified by Anderson et al. (2014) (see Fig. 2). In projection, the G323.18+0.15 complex lies to the west of the largest H_{II} region G323.349+0.205 (traced by the largest white circle), and is close to the H_{II} region G323.101+0.268 (traced by the second largest white circle). The G323.18+0.15 complex seems to be on the rim of the 21 cm continuum emission. However, the velocity distribution in the top right panel of Fig. 5 does not show an increasing velocity gradient along the expanding direction of the H_{II} region (from east to west). Fig. 2 shows that almost all class I YSOs lie along the U-shape structure G323.18b. Most class II YSOs are located in or nearby the region covered by G323.18ab. They do not lie along the left side of complex G323.18+0.15, where interaction may have taken place. This indicates that the largest H_{II} region may not strongly interact with complex G323.18+0.15, but we cannot rule out the possibility that some class II YSOs may be formed due to triggered star formation induced by the largest H_{II} region. The G323.18+0.15 complex as a whole shows a filamentary structure that is nearly parallel to the expanding direction of the second largest H_{II} region (Fig. 2). G323.18a is

closest to the H_{II} region and shows no evidence of being compressed by it, while G323.18b and G323.18c are far away from it. Therefore complex G323.18+0.15 is probably not affected by the second largest H_{II} region.

Due to the presence of the H_{III} region in between filaments G323.18c and G323.18ab, we have to consider that the compression could be caused by the expansion of this H_{II} region into the gas. The H_{II} region G323.187+00.129 has a size of about 2.84 pc. Our study of small bubbles with similar size, N22 (Ji et al. 2012) and N10 (Ma et al. 2013), suggests that the region may have a kinematic age younger than 1 Myr. The collect-and-collapse model of triggered star formation may not work for the H_{II} region G323.187+00.129, that is, it has not had enough time to collect the surrounding materials and form compressed layers, and then to collapse to form clumps or cores and stars. As Fig. 6 shows, G323.18ab covers nearly half of the H_{II} region in projection, but no compressed CO or dust shells appear along the edge of the H_{II} region. However, the northwestern part of G323.18c shows some evidence of being compressed by the H_{II} region. This is consistent with the idea we described in sect. 4.3.

5. Conclusions

The structure and kinematics of the G323.18+0.15 complex has been studied, and strong evidence is found that supports the hypothesis that a CCC occurred between the cloud components G323.18a and G323.18bc. Our results are listed below.

1. The G323.18a - G323.18b structure as a whole is probably not gravitationally bound, suggesting that any star formation in these clouds has been triggered by an accident. A reasonable explanation is that the smaller cloud G323.18a collides with the larger cloud G323.18bc, which forms a U-shape structure and a dense compressed layer in G323.18b. The column density of the compressed layer is estimated at $1.36 \times 10^{22} \text{ cm}^{-2}$, which satisfies the threshold condition for forming high-mass stars.
2. G323.18b appears as a perfect U-shape structure showing an enhanced velocity dispersion. The shape of the G323.18a structure complements the U-shape structure found in G323.18b. Except for these two typical features of a CCC, the bridge feature with an intermediate velocity be-

tween G323.18a and G323.18b also supports the hypothesis that they collide.

3. A total of 46 YSOs were found to be distributed in the region we studied. The average surface density of class I and class II YSOs in the region covered by G323.18a and G323.18b is about 0.39 and 0.58 arcmin⁻², respectively, which is much higher than for the surrounding regions. The timescale of the collision of G323.18a and G323.18b is estimated to be 1.59 Myr, which is longer than the typical lifetime of class I YSOs and is comparable to the lifetime of class II YSOs. Almost all class I YSOs are associated with the U-shape structure and suggest a CCC-related origin.

Acknowledgements. The authors thank the anonymous referee for helpful comments. This work was mainly funded by the National Natural Science foundation of China (NSFC) under grant No.11973076. It was also partially supported by the NSFC under grant Nos.11433008, 11903070, 12173075, and 12103082, the Heaven Lake Hundred Talent Program of Xinjiang Uyghur Autonomous Region of China, the Natural Science Foundation of Xinjiang Uygur Autonomous Region under grant No. 2022D01E06, and the CAS Light of West China Program under grant Nos. 2020-XBQNXZ-017 and 2021-XBQNXZ-028. D. L. Li has been funded by Youth Innovation Promotion Association CAS and Tianshan Innovation Team Plan of Xinjiang Uygur Autonomous Region (2022D14020). Y. X. has been funded by High Level Talent Heaven Lake Program of Xinjiang Uyghur Autonomous Region of China. W. B. has been funded by Chinese Academy of Sciences President's International Fellowship Initiative by Grant No. 2021VMA0008.

References

- Anathpindika, S. V. 2010, MNRAS, 405, 1431
 Anderson, L. D., Bania, T. M., Balsler, D. S., et al. 2014, ApJS, 212, 1
 Aniano, G., Draine, B. T., Gordon, K. D., & Sandstrom, K. 2011, PASP, 123, 1218
 Ascenso, J. 2018, in *Astrophysics and Space Science Library*, Vol. 424, *The Birth of Star Clusters*, ed. S. Stahler, 1
 Bonnell, I. A., Bate, M. R., Clarke, C. J., & Pringle, J. E. 2001, MNRAS, 323, 785
 Burton, M. G., Braiding, C., Glueck, C., et al. 2013, PASA, 30, e044
 Carey, S. J., Noriega-Crespo, A., Mizuno, D. R., et al. 2009, PASP, 121, 76
 Churchwell, E., Babler, B. L., Meade, M. R., et al. 2009, PASP, 121, 213
 Dunham, M. M., Allen, L. E., Evans, Neal J., I., et al. 2015, ApJS, 220, 11
 Elia, D., Molinari, S., Schisano, E., et al. 2017, MNRAS, 471, 100
 Evans, Neal J., I., Dunham, M. M., Jørgensen, J. K., et al. 2009, ApJS, 181, 321
 Fazio, G. G., Hora, J. L., Allen, L. E., et al. 2004, ApJS, 154, 10
 Fukui, Y., Habe, A., Inoue, T., Enokiyama, R., & Tachihara, K. 2020, PASJ[arXiv:2009.05077]
 Fukui, Y., Harada, R., Tokuda, K., et al. 2015, ApJ, 807, L4
 Fukui, Y., Ohama, A., Hanaoka, N., et al. 2014, ApJ, 780, 36
 Fukui, Y., Torii, K., Hattori, Y., et al. 2018, ApJ, 859, 166
 Gong, Y., Fang, M., Mao, R., et al. 2017, ApJ, 835, L14
 Gutermuth, R. A., Megeath, S. T., Myers, P. C., et al. 2009, ApJS, 184, 18
 Habe, A. & Ohta, K. 1992, PASJ, 44, 203
 Haverkorn, M., Gaensler, B. M., McClure-Griffiths, N. M., Dickey, J. M., & Green, A. J. 2006, ApJS, 167, 230
 Haworth, T. J., Shima, K., Tasker, E. J., et al. 2015a, MNRAS, 454, 1634
 Haworth, T. J., Tasker, E. J., Fukui, Y., et al. 2015b, MNRAS, 450, 10
 Inoue, T. & Fukui, Y. 2013, ApJ, 774, L31
 Issac, N., Tej, A., Liu, T., & Wu, Y. 2020, MNRAS, 499, 3620
 Ji, W. G., Zhou, J. J., Esimbek, J., et al. 2012, A&A, 544, A39
 Kauffmann, J., Bertoldi, F., Bourke, T. L., Evans, N. J., I., & Lee, C. W. 2008, A&A, 487, 993
 Krumholz, M. R., Klein, R. I., & McKee, C. F. 2012, ApJ, 754, 71
 Krumholz, M. R., Klein, R. I., McKee, C. F., Offner, S. S. R., & Cunningham, A. J. 2009, Science, 323, 754
 Li, G.-X., Urquhart, J. S., Leurini, S., et al. 2016, A&A, 591, A5
 Liu, H.-L., Wu, Y., Li, J., et al. 2015, ApJ, 798, 30
 Ma, Y., Zhou, J., Esimbek, J., et al. 2013, Ap&SS, 345, 297
 McKee, C. F. & Tan, J. C. 2002, Nature, 416, 59
 Molinari, S., Swinyard, B., Bally, J., et al. 2010, PASP, 122, 314
 Ossenkopf, V. & Henning, T. 1994, A&A, 291, 943
 Pillai, T., Kauffmann, J., Wyrowski, F., et al. 2011, A&A, 530, A118
 Reid, M. J., Menten, K. M., Brunthaler, A., et al. 2019, ApJ, 885, 131
 Rieke, G. H., Young, E. T., Engelbracht, C. W., et al. 2004, ApJS, 154, 25
 Schuller, F., Urquhart, J. S., Csengeri, T., et al. 2021, MNRAS, 500, 3064
 Takahira, K., Shima, K., Habe, A., & Tasker, E. J. 2018, PASJ, 70, S58
 Takahira, K., Tasker, E. J., & Habe, A. 2014, ApJ, 792, 63
 Urquhart, J. S., König, C., Giannetti, A., et al. 2018, MNRAS, 473, 1059
 Urquhart, J. S., Moore, T. J. T., Csengeri, T., et al. 2014, MNRAS, 443, 1555
 Wang, K., Testi, L., Ginsburg, A., et al. 2015, MNRAS, 450, 4043
 Zhou, J., Zhou, D., Esimbek, J., et al. 2020, ApJ, 897, 74
 Zinnecker, H. & Yorke, H. W. 2007, ARA&A, 45, 481

Table 1. Parameters of dust cores associated with G323.18+0.15. The first, second, and third columns list the names, diameters, and masses of the clumps in the Herschel Hi-Gal clump catalog. The fourth and fifth columns indicate the evolutionary stage of the clumps and whether it is located within the G323.18+0.15 complex. The sixth and seventh columns indicate the new diameters and masses calculated for a distance of 3.55 kpc. The eighth column presents the clump surface density. AGAL323.104+0.024, AGAL323.192+0.154, and AGAL323.171+0.139 are the clumps that fall into the G323.18+0.15 complex in the ATLASGAL dense clump catalog. The sources AGAL323.104+0.024, AGAL323.192+0.154, HIGALBM323.1050+0.0241, and HIGALBM323.1923+0.1539 are duplicated.

Name	Diam pc	Mass M_{\odot}	Evol	in/out	Diam(new) pc	Mass(new) M_{\odot}	surface density g cm^{-2}
HIGALBM323.0365+0.1431	1.158	425.61	prestellar	out			
HIGALBM323.0672+0.2635	0.471	409.01	protostellar	out			
HIGALBM323.0673+0.1090	1.270	1079.55	protostellar	out			
HIGALBM323.0698+0.0501	1.463	2190.30	prestellar	out			
HIGALBM323.1050+0.0241 (AGAL323.104+0.024)	0.816	510.81	prestellar	out			
HIGALBM323.1205+0.1452	1.151	1436.53	prestellar	out			
HIGALBM323.1243+0.0505	1.885	5153.03	prestellar	out			
HIGALBM323.1379+0.1743	0.481	307.05	prestellar	in	0.393	204.97	0.35
HIGALBM323.1393+0.0916	1.079	1063.05	prestellar	out			
HIGALBM323.1437+0.1600	0.921	1771.21	prestellar	in	0.350	256.37	0.56
HIGALBM323.1605+0.1387	1.392	11753.03	prestellar	in	0.530	1701.18	1.62
HIGALBM323.1915+0.1151	1.157	508.43	protostellar	in	0.439	73.28	0.10
HIGALBM323.1923+0.1539 (AGAL323.192+0.154)	0.614	535.31	protostellar	in	0.233	77.15	0.38
HIGALBM323.1990+0.1106	0.916	1483.38	protostellar	in	0.348	213.79	0.47
HIGALBM323.2032+0.0808	1.538	1350.40	prestellar	in	0.464	122.81	0.15
HIGALBM323.2044+0.1582	0.530	314.52	protostellar	in	0.201	45.33	0.30
HIGALBM323.2168+0.1870	1.567	134.32	protostellar	in	0.481	12.65	0.01
HIGALBM323.2181+0.0529	1.697	1102.78	prestellar	in	0.512	100.29	0.10
HIGALBM323.2182+0.0362	1.445	1626.27	prestellar	in	0.436	147.89	0.21
HIGALBM323.2194+0.1907	1.479	1014.20	protostellar	in	0.454	95.50	0.12
HIGALBM323.2273+0.1433	1.119	3038.81	prestellar	out			
AGAL323.171+0.139	0.468	749.89	YSO	in	0.413	584.79	0.92

Appendix A: Young star classification

First, we selected the candidates that are located in the G323.18+0.15 complex and have photometric detections in all four IRAC bands ($\sigma < 0.2$ mag) from the GLIMPSE I Spring 07 highly reliable catalog. Then we removed sources contaminated by polycyclic aromatic hydrocarbons according to the constraints from Gutermuth et al. (2009): $[3.6] - [4.5] - \sigma \leq 1.4 \times (([4.5] - [5.8]) + \sigma_1 - 0.7) + 0.15$ and $[3.6] - [4.5] - \sigma_2 < 1.65$, where $\sigma_1 = \sigma \{[4.5] - [5.8]\}$ and $\sigma_2 = \sigma \{[3.6] - [4.5]\}$. Finally, we identified 16 class I YSOs following the constraints $[4.5] - [5.8] > 0.7$ and $[3.6] - [4.5] > 0.7$, and 12 class II YSOs following the constraints $[4.5] - [8.0] - \sigma_3 > 0.5$, $[3.6] - [5.8] - \sigma_4 > 0.35$, $[3.6] - [5.8] + \sigma_4 \leq 3.5 \times (([4.5] - [8.0]) - \sigma_3) - 0.5 + 0.5$, and $[3.6] - [4.5] - \sigma_2 > 0.15$, where $\sigma_3 = \sigma \{[4.5] - [8.0]\}$ and $\sigma_4 = \sigma \{[3.6] - [5.8]\}$. Four sources lack detections at either 5.8 or 8.0 μm but with 3.6 and 4.5 μm with $\sigma < 0.2$ mag and H and K bands from 2MASS with $\sigma < 0.1$ mag in our region. We identified 24 class II YSOs following the constraints $[[3.6] - [4.5]]_0 - \sigma_1 > 0.101$, $[K - [3.6]]_0 - \sigma_2 > 0$, $[K - [3.6]]_0 - \sigma_2 > -2.85714 \times ([3.6] - [4.5]]_0 - \sigma_1 - 0.101) + 0.5$, and $[3.6]_0 < 14.5$ where $\sigma_1 = \sigma \{[3.6] - [4.5]\}_{\text{meas}}$ and $\sigma_2 = \sigma \{[K] - [3.6]\}_{\text{meas}}$ (Gutermuth et al. 2009). We used MIPS 24 μm with magnitude [24] < 7 ($\sigma < 0.2$ mag) to identify transition disks (TDs) following the criteria $[5.8] - [24] > 2.5$ or $[4.5] - [24] > 2.5$, and $[3.6] < 14$. The TDs are classified as sources in an evolutionary stage between class II and class III (Gutermuth et al. 2009), but no TD was found in our G323.18+0.15 complex. The absence of a TD suggests that star formation in G323.18+0.15 is in its early stage, and perhaps the CCC between G32.18a and G323.18b led to a rapid increase of mass at the interface of the collision, and was followed by star formation in a short time.